SPECIAL DIAMET COLLECTION

Precipitation Banding in Idealized Baroclinic Waves

JESSE NORRIS, GERAINT VAUGHAN, AND DAVID M. SCHULTZ

Centre for Atmospheric Science, School of Earth, Atmospheric and Environmental Sciences, University of Manchester, Manchester, United Kingdom

(Manuscript received 25 October 2013, in final form 24 March 2014)

ABSTRACT

Moist idealized baroclinic-wave simulations show the development of precipitation bands from a zonally uniform initial midlatitude jet. For a frictionless lower boundary, and with no latent-heat release or surface heat and moisture fluxes, warm advection is strong and a bent-back warm front forms. Although a narrow vertical-velocity maximum forms within the area of synoptic-scale ascent near the triple point, only a wide warm-frontal band forms. As surface roughness length increases between simulations to that of an ocean then a land surface, warm advection is reduced and the cold front becomes stronger relative to the warm front. A separate narrow rainband forms along the cold front, which is more intense and farther removed from the wide warm-frontal band when roughness length is greater. In the simulation with roughness length appropriate to the ocean, after the narrow band decays, the precipitation becomes oriented along the warm conveyor belt in the warm sector. When latent-heat release is included, this warm-sector precipitation evolves into multiple bands, which eventually weaken with the cyclone. When surface heat and moisture fluxes are included, the ascent at the surface cold front stays strong and a well-defined cold front of the anafront variety persists through this mature stage. The surface precipitation remains in a single intense band along and ahead of the cold front. Therefore, strong surface heat and moisture fluxes inhibit multiple bands, but a simulation with lower sea surface temperature (SST) more closely resembles the simulation without surface heat and moisture fluxes, demonstrating that the detailed structure and evolution of precipitation banding is sensitive to SST.

1. Introduction

Heavy precipitation within extratropical cyclones is often organized into mesoscale bands (e.g., Houze et al. 1976; Hobbs 1978; Houze and Hobbs 1982; Browning 1986, 1990, 2005; Browning et al. 1997; Browning and Roberts 1999). Houze and Hobbs (1982) classified precipitation bands by where they occur in extratropical cyclones, producing a conceptual model featuring six different types of precipitation bands: warm frontal, warm sector, wide cold frontal, narrow cold frontal, prefrontal cold surge, and postfrontal. Many of these types of precipitation bands are associated with airstreams within extratropical cyclones called conveyor belts (Carlson 1980; Browning 1986). Thus, the Houze and Hobbs (1982) conceptual model serves as a template against which both observational and modeling studies can categorize bands within extratropical cyclones.

However, not all of these six types of bands appear within all cyclones. For example, Parsons and Hobbs (1983) documented five cyclones over the eastern North Pacific Ocean, all of which exhibited wide and narrow cold-frontal rainbands, but none of which exhibited warm-frontal bands. Such cold fronts are sometimes referred to as ana-type fronts, where the moist air in the warm conveyor belt rises abruptly up the front (e.g., Browning and Pardoe 1973; James and Browning 1979; Browning 1986). Conversely, other cyclones favor banding in the warm sector and along the warm front (e.g., Browning et al. 1973;

Denotes Open Access content.

Corresponding author address: Jesse Norris, Earth Research Institute, University of California, Santa Barbara, 4704 Ellison Hall, Santa Barbara, CA 93106-3060.
E-mail: jesse.norris@ucsb.edu

DOI: 10.1175/MWR-D-13-00343.1

Publisher's Note: This article was revised on 10 November 2014 to include the CCBY license designation that was missing when originally published.

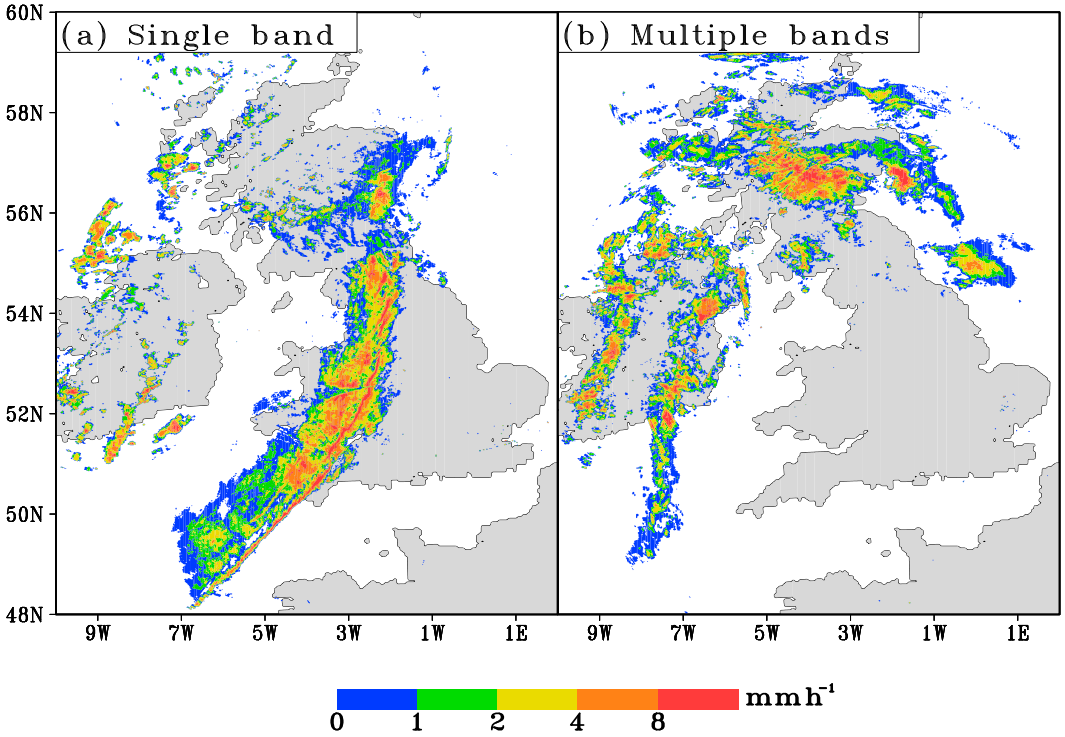

FIG. 1. Met Office precipitation-radar composites at 1-km grid spacing, expressed as precipitation rate in mm h^{-1} during the passage of fronts over the British Isles: (a) a single band at 1600 UTC 22 Nov 2012 and (b) multiple bands at 0330 UTC 19 Nov 2012. In (a), the leading edge of the wide band over England and Wales corresponds to the analyzed cold front on the Deutscher Wetterdienst chart (http://www.wetter3.de/Archiv/archiv_dwd.html). In (b), the rearmost band, over western Ireland, corresponds to the analyzed cold front on the Deutscher Wetterdienst chart.

Heymsfield 1979; Novak et al. 2004). Such cyclones are sometimes considered to contain kata-type cold fronts, where the air in the warm conveyor belt rises ahead of the cold front and the surface cold front is overrun by dry air from the stratosphere and upper troposphere (e.g., Bergeron 1937; Sansom 1951; Browning and Monk 1982). In addition, precipitation sometimes remains within a single wide band along a front, albeit with multiple lines of embedded features (Fig. 1a). But often, even if only a single front is analyzed, the frontal precipitation separates into multiple parallel bands of similar width and intensity (Fig. 1b). These examples demonstrate the considerable variety of precipitation structures within extratropical cyclones.

Previous research has identified a number of factors controlling the structure and evolution of banded features along fronts. For example, nonuniformities in the initial temperature gradient may result in the production of multiple fronts in an idealized baroclinic wave (Hoskins et al. 1984). However, such nonuniformities are not required to produce multiple bands. Even in two-dimensional (e.g., Knight and Hobbs 1988; Bénard et al. 1992a; Xu 1992; Pizzamei et al. 2005) and three-dimensional (e.g., Zhang and Cho 1995; Gray and Dacre 2008) idealized model simulations, fronts with an initial single maximum of vertical velocity may develop multiple maxima of vertical velocity over time.

These observations and modeling results motivate the questions of what causes precipitation bands in cyclones and what determines whether they are singly or multiply banded. Bennetts and Hoskins (1979) suggested that frontal rainbands form when latent-heat release renders the atmosphere symmetrically unstable to saturated ascent (so-called conditional symmetric instability, CSI), apparently supported by some observational studies (e.g., Seltzer et al. 1985; Wolfsberg et al. 1986). Schultz and Schumacher (1999) reviewed the literature and found that even if a region of the atmosphere meets the criteria for CSI, banded precipitation may or may not occur, results since confirmed by other studies (e.g., Schultz and Knox 2007; Novak et al. 2010; Schumacher et al. 2010).

The formation, movement, and dissipation of precipitation bands sometimes differ dramatically between high-resolution numerical weather prediction model output and observed radar data (e.g., Novak and Colle 2012). Thus, any improvement in understanding the factors that affect their formation and evolution may be helpful in improving weather forecasts. Despite the research described above, what has not been examined to date within the context of

three-dimensional idealized baroclinic waves is the sensitivity of the bands to diabatic processes such as surface friction, latent-heat release, and surface heat and moisture fluxes.

The purpose of this paper is to examine the formation and evolution of banded precipitation within idealized baroclinic waves to better understand their sensitivity to diabatic processes, specifically surface friction, the release of latent heat, and surface heat and moisture fluxes. To address these issues, a three-dimensional primitive equation model is used to simulate precipitation bands within an idealized baroclinic wave. Our motivation is to demonstrate how precipitation banding evolves within the cyclone, free from the complications of real-data cases, such as orography, land–sea differences, and case-to-case variability. A control simulation over the ocean without latent-heat release or surface heat and moisture fluxes is compared to other simulations in which the roughness length of the lower boundary is varied, and the release of latent heat and the surface heat and moisture fluxes are included. Thus, this paper demonstrates how these diabatic processes affect the structure and evolution of precipitation banding in extratropical cyclones.

The remainder of this article is organized as follows. Section 2 details the mesoscale model and initial conditions used to simulate idealized baroclinic waves and explains the modeling strategy, specifically the sensitivity experiments to be performed. The results of the simulations are presented in the next four sections. Section 3 documents the formation of precipitation bands in the control simulation. Section 4 explores the effect that varying roughness length has on the bands. Section 5 examines how the release of latent heat affects the formation of multiple bands. Section 6 examines the effect of varying the magnitude of surface heat and moisture fluxes on the formation of multiple bands. Section 7 compares our simulations to previously published observations of precipitation bands to understand the generality of our results. Section 8 concludes this article.

2. Model setup

Moist idealized baroclinic-wave simulations were performed with version 3.4.1 of the Advanced Research core of the Weather Research and Forecasting Model (ARW-WRF; Skamarock et al. 2008, hereafter just WRF). The model was initialized by the WRF baroclinic-wave test case, which consists of a zonal jet of roughly 20 K $(1000\,\mathrm{km})^{-1}$ at the surface, spanning 8000 km from north to south on an f plane (where $f = 10^{-4}\,\mathrm{s}^{-1}$ is the Coriolis parameter) in thermal wind balance. The jet is obtained by inverting a baroclinically unstable potential vorticity (PV) distribution on the y–z plane, as in Rotunno et al. (1994). The domain is periodic from west to east and simulations were performed with a wavelength of 4000 km, which is the wavelength of the most unstable normal mode of the WRF initial jet [Plougonven and Snyder (2007), whose initial conditions this study uses]. The focus in this present paper is on the organization of bands spaced a few hundreds of kilometers apart (e.g., Fig. 1b), so 20-km grid spacing was chosen with 80 vertical levels from the surface up to 16 km. The simulations were run for 204 h with a time step of 120 s.

To investigate how bands may form over a zonally homogeneous ocean surface, a control simulation, OCEANFRIC, is chosen with roughness length appropriate to the ocean (with surface momentum fluxes calculated and diffused into the free atmosphere by surface-layer and boundary layer parameterizations) and microphysics, but with all latent-heat rates set to zero (Table 1). In subsequent simulations, the roughness length is varied (where surface-layer and boundary layer parameterizations are used if and only if the roughness length is nonzero) and latent-heat release, then surface heat and moisture fluxes (hereafter, just "surface fluxes"), are incrementally switched on (Table 2). In this way, the impact of each of these diabatic effects on band formation can be isolated.

The magnitude of the roughness length controlled the preocclusion stage of the cyclone's development and formation of its fronts. To showcase this sensitivity to roughness length, section 3 presents the early evolution of precipitation bands in OCEANFRIC, and section 4 compares NOFRIC, OCEANFRIC, and LANDFRIC, which differ only in their roughness lengths. In the simulations where friction was included, a constant value of the roughness length was prescribed across the whole domain, equal to 0.2 and 200 mm for ocean (OCEANFRIC) and land (LANDFRIC), respectively, following Hines and Mechoso (1993). In these three simulations, an inner domain of 4-km grid spacing with a 24-s time step was inserted during this preocclusion stage because one band of interest at this stage of the simulations was poorly resolved at 20-km grid spacing. The output of these inner domains is only briefly discussed and plotted in section 4b, before the remainder of the manuscript documents the output at 20-km grid spacing (which is the focus of this paper and is unaffected by the inner domain due to one-way interaction between the two domains).

The effects of including latent-heat release and surface fluxes were most evident in the mature stage of the cyclone. The LATENT and FLUX simulations (in which latent heat and surface fluxes are included incrementally from OCEANFRIC) are presented in sections 5 and 6, respectively. In FLUX, the first simulation in which surface fluxes were active, a sea surface temperature (SST) distribution was prescribed equal to the initial temperature of the lowest model level, following Adamson et al. (2006). Another simulation, FLUX–10, is presented in section 6, which is equivalent to FLUX, but

TABLE 1. Parameterizations in OCEANFRIC. Additional simulations employed the same parameterizations, but with varying roughness length, latent-heat release included in the microphysics (in which case, cumulus parameterization was also used, which the model requires to be switched off when latent heating is excluded from the microphysics), and surface heat and moisture fluxes included in the surface-layer parameterization, as detailed in Table 2. MM5: Fifth-generation Pennsylvania State University–National Center for Atmospheric Research Mesoscale Model.

Microphysics	Thompson et al. (2008), but with all latent-heat rates zero
Surface layer	MM5; Monin and Obukhov (1954), excluding surface heat and moisture fluxes
Boundary layer	Yonsei University (Hong et al. 2006)

TABLE 2. A summary of all simulations. Gives roughness length z_0, whether latent heating (LH) was active (Y) or turned off (N), the SST distribution (for simulations with this entry blank, surface heat and moisture fluxes were switched off; T_0 is the initial temperature of the lowest model level) and in which section(s) results are presented. In all simulations in which latent heat was switched on, the Kain–Fritsch cumulus scheme (Kain 2004) was also included.

	z_0 (mm)	LH	SST	Section
OCEANFRIC	0.2	N	—	3–5
NOFRIC	0	N	—	4
LANDFRIC	200	N	—	4
LATENT	0.2	Y	—	5, 6
FLUX	0.2	Y	T_0	6
FLUX–10	0.2	Y	$T_0 - 10$ K	6

with a SST distribution with 10 K subtracted from each grid point.

These simulations are not fully representative of extratropical cyclones over ocean and land. In particular, there is no land surface or radiation parameterization, hence no diurnal effects, which, particularly over land, may be expected to influence cyclones in the real atmosphere. However, the purpose of this paper is not to perform full-physics baroclinic-wave simulations, but rather to isolate the effects on precipitation bands of roughness length (NOFRIC, OCEANFRIC, and LANDFRIC), latent-heat release (OCEANFRIC versus LATENT), and surface fluxes (LATENT, FLUX, and FLUX–10).

3. Formation of precipitation bands in the control simulation

We now look at the preocclusion stage of baroclinic-wave development, and the formation of vertical-velocity maxima and precipitation bands. Section 3a gives an overview of OCEANFRIC (the control simulation, which has a roughness length appropriate to the ocean) and the evolution of its bands. Section 3b looks more closely at the mechanisms by which the vertical-velocity maxima and precipitation bands initially form.

a. *Overview of control simulation*

The low center deepens primarily between about 90 and 144 h (Fig. 2a, crisscrosses on the OCEANFRIC curve), which is also the period during which the surface-θ gradient intensifies (Fig. 2b, crisscrosses on the OCEANFRIC curve). Figure 3 shows the evolution of the system during this period.

Initially, a single band of synoptic-scale precipitation lies over the developing surface warm front (Fig. 3a), corresponding to a single wide maximum of vertical velocity throughout the troposphere (Fig. 3b, w1). Then, a narrow maximum of vertical velocity, w2, begins to separate from w1 (Fig. 3d), originating at the triple point of the cyclone (Fig. 3c). The wide precipitation band subsequently develops equatorward and, although not producing a rainband, w2 also develops equatorward at the leading edge of the cold advection (Figs. 3e,f). By 132 h, a wide vertical-velocity maximum, w3, has formed above and behind the surface cold front, but is in the dry air above the cloud head (Fig. 3f) and so does not lead to precipitation (Fig. 3e).

After 144 h, the surface cold front has become well defined at the equatorward end of the wide precipitation band and there is a poorly defined narrow rainband along this part of the cold front (Fig. 3g), through which the cross section passes. The narrow band is where w2 has become of greater magnitude, more vertically oriented, and more clearly separated from w1 (Fig. 3h). Although w2 is well resolved in this simulation, 20-km grid spacing is insufficient to resolve the associated rainband, as will be illustrated in section 4b. This time is the closest that a cold-frontal rainband comes to forming in this simulation.

The above vertical-velocity maxima are similar to those in previous idealized modeling studies. The wide warm-frontal vertical-velocity maximum, w1, resembles the warm-sector-wide vertical-velocity band[1] simulated by Knight and Hobbs (1988) and Bénard et al. (1992a). The narrow cold-frontal maximum, w2, resembles the narrow surface-cold-frontal bands of vertical velocity simulated by Knight and Hobbs (1988), Bénard et al. (1992a), and Zhang and Cho (1995). The wide cold-frontal vertical-velocity maximum, w3, resembles the wide cold-frontal band of vertical velocity simulated by Bénard et al. (1992a).

b. *Initial band formation*

We now look at the details of OCEANFRIC during this formative period, specifically how the model

[1] When referring to the simulations presented in this paper, "band" is used exclusively for a precipitation band, but we refer to previous authors' "bands" of vertical velocity where they have so termed them.

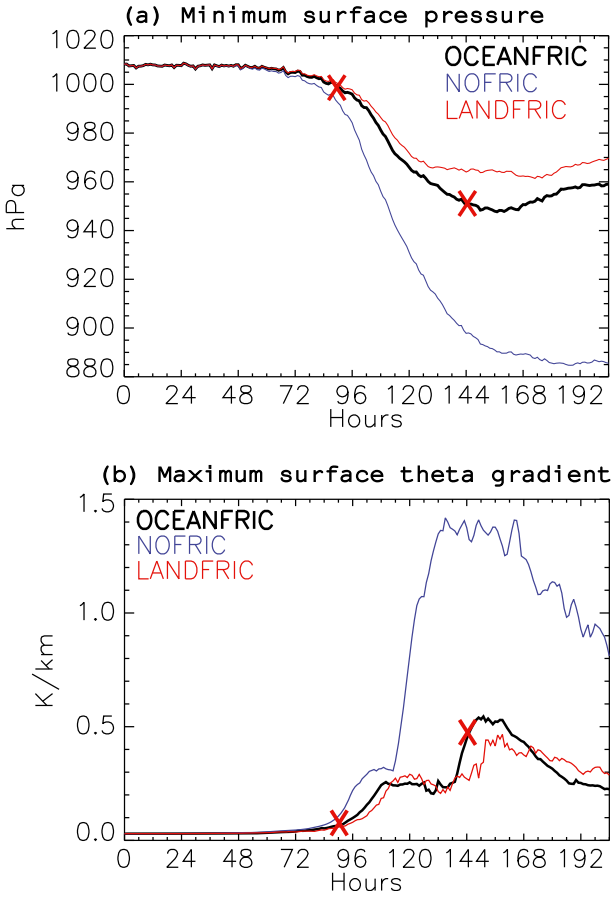

FIG. 2. Time series of (a) domain minimum surface pressure and (b) domain maximum surface potential temperature gradient for three simulations of varying roughness length. Surface is defined as the lowest model level (sea level, due to absence of orography). Values are obtained for every hour of the simulations. Surface potential temperature gradient is calculated by $[(\theta_{i+1,j} - \theta_{i-1,j})^2 + (\theta_{i,j+1} - \theta_{i,j-1})^2]^{1/2}/2\Delta x$, where θ is potential temperature; the $_i$ and $_j$ subscripts denote the zonal and meridional grid coordinates, respectively; and $\Delta x = 20$ km is the grid spacing. Crisscrosses on the OCEANFRIC curves in each panel mark the period covered in Fig. 3.

generates the different vertical-velocity maxima. Closer inspection of the developing fronts, before any of the additional vertical-velocity maxima and precipitation bands in Fig. 3 have formed, shows a weak maximum of surface–850-hPa mean lapse rate (hereafter, just "lapse rate") lying above the developing cold front and warm sector (Fig. 4a). A cross section across the developing cold front demonstrates that the shallow postfrontal boundary layer is absolutely unstable (Fig. 4b). However, at this time, there is descent where there is cold advection (Fig. 4b) and ascent where there is warm advection (Fig. 4c, the w1 maximum in Fig. 3), as explained by quasigeostrophic theory (Holton and Hakim 2013, chapter 6). Therefore, the ascent and instability are separated from one another and so there is no lift to release the instability.

Six hours later, the lapse-rate maximum lies closer to the wide precipitation band than before (Fig. 4d). Thus, the cold- and warm-frontal cross sections collectively reveal that the unstable postfrontal boundary layer and warm-frontal ascent have come closer together, so that a maximum within the ascent, w2, begins to form near the triple point (Figs. 4e,f). This moment marks the formation of the w2 maximum shown in Fig. 3, which eventually forms the poorly defined narrow rainband.

Another 12 h later, the lapse-rate maximum has narrowed and intensified as the warm sector becomes narrower (Fig. 4g). The postfrontal boundary layer is well defined and much more unstable than before, so that w2 has also intensified (Fig. 4h). Furthermore, the wide cold-frontal w3 maximum shown in Fig. 3 has formed in conjunction with a midlevel trough (not shown), so that there is large-scale ascent up the cold front, where there was previously large-scale descent (cf. Figs. 4e,h).

Thus, the model first produces w1 from synoptic-scale warm advection, then w2 at the surface cold front, as a narrow instability maximum forms near the triple point, within the synoptic-scale ascent, and finally w3 as a midlevel trough forms above and behind the surface cold front. However, in OCEANFRIC, these vertical-velocity maxima do not produce well-defined multiple precipitation bands. Sections 4–6 show that variations in roughness length, and switching on latent-heat release and surface fluxes, can result in multiple precipitation bands from these and other vertical-velocity maxima.

4. Effects of roughness length on precipitation bands

NOFRIC and LANDFRIC are now compared to OCEANFRIC, during the period documented in section 3. Roughness length affects the large-scale structure of the baroclinic wave in these simulations, and so section 4a first documents the differences in the cyclone structure between the simulations, which is required to explain the effects of roughness length on the precipitation bands, presented in section 4b.

a. Sensitivity of cyclone structure to roughness length

In simulations with greater roughness length, the cyclone deepens more slowly and is less intense: the minimum central pressures are 883, 948, and 961 hPa in NOFRIC, OCEANFRIC, and LANDFRIC, respectively (Fig. 2a). The maximum surface-θ gradient is also less for simulations with greater roughness length (Fig. 2b), particularly the warm front, which in OCEANFRIC reaches only 19% of the magnitude that it does in NOFRIC (as calculated in Fig. 5). The cold front is less affected, which in OCEANFRIC reaches 38% of its magnitude in

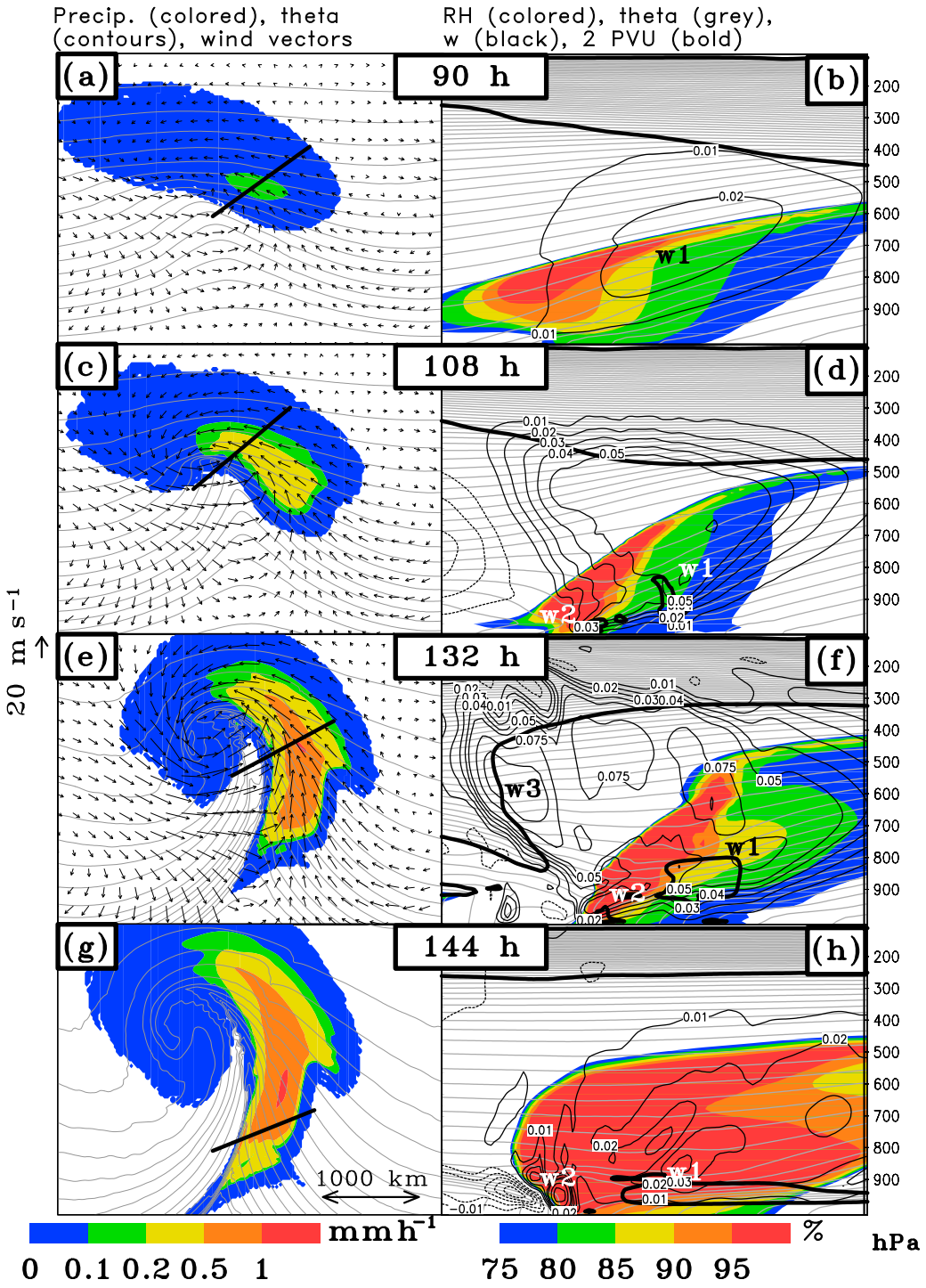

FIG. 3. Evolution of OCEANFRIC, between 90 and 144 h, showing, at given times into the simulation the (a),(c),(e),(g) surface precipitation rate (colored, mm h^{-1}), θ (gray contours every 3 K), and wind vectors (m s^{-1}). Domain is recentered around the precipitation distribution, as in all horizontal plots in this paper. (b),(d),(f),(h) Cross sections at locations indicated by straight line in left-hand panel, showing relative humidity (colored, %), w (labeled black contours at ±0.01, ±0.02, ±0.03, ±0.04, ±0.05, ±0.075, and ±0.1 m s^{-1}; negative contours dashed), θ (gray contours every 3 K), and the dry-PV 2-potential vorticity unit (PVU) contour (1 PVU = 10^{-6} K kg^{-1} m^2 s^{-1}; thick solid lines). Wind vectors are not drawn in (g) for clarity of precipitation features. Important w maxima are numbered in cross sections and numbers correspond between panels and to subsequent cross sections (e.g., w1 is the same w maximum throughout the paper). Note, the low-level PV in (d),(f),(h) (and subsequent cross sections throughout this paper) is not diabatic, but due to the strong numerical diffusivity in grid boxes in frontal zones above a no-slip boundary (Cooper et al. 1992).

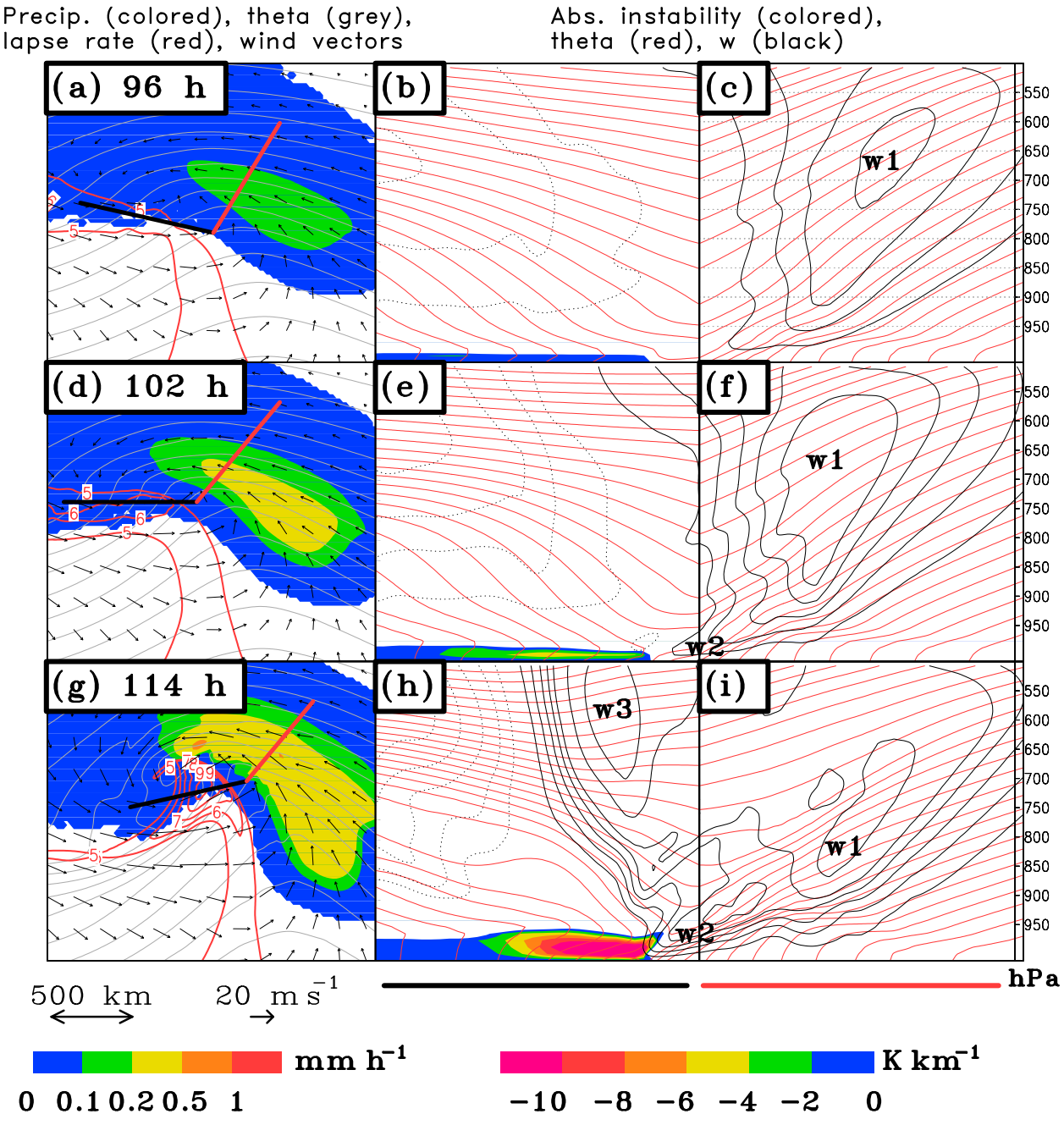

FIG. 4. Finer-scale evolution of OCEANFRIC at given times. (a),(d),(g) As in Fig. 3, but also showing labeled red contours of mean surface–850-hPa lapse rate (K km^{-1}), calculated by $(T_{\rm surf} - T_{850})/(z_{850} - z_{\rm surf})$, where T and z are temperature and height, respectively, and the "surf" and "850" subscripts denote the lowest model level and the 850-hPa hydrostatic pressure level, respectively. (b),(e),(h) and (c),(f),(i) Cross sections across cold and warm fronts, respectively, at locations indicated in the left-hand panels by black and red straight lines, respectively, meeting in the warm sector. Cross sections are as in the right-hand panels in Fig. 3, but only extending to 500 hPa, θ contours are red and their interval is reduced to 2 K, and no relative humidity or PV is drawn, instead showing negative $\partial\theta/\partial z$ (colored, K km^{-1}), indicating absolute instability.

NOFRIC. The difference in frontal contrast between simulations of different roughness length is because wind speed in the warm sector reduces as roughness length increases, which further reduces frontogenesis along the warm front through the feedback between synoptic-scale forcing and vertical motion (e.g., Hines and Mechoso 1993; Rotunno et al. 1998). Frontogenesis along the cold front, on the other hand, occurs away from the low center, where Ekman pumping is weaker (Rotunno et al. 1998). Hence, postfrontal wind speed is less affected by

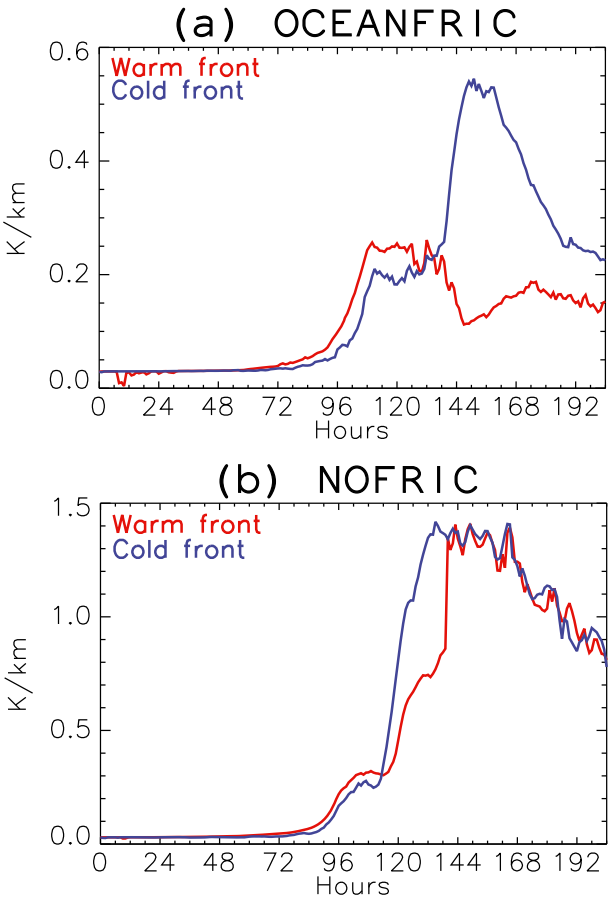

FIG. 5. Time series of maximum surface potential temperature gradient (as defined in Fig. 2 caption) along cold and warm fronts in (a) OCEANFRIC and (b) NOFRIC. Cold and warm fronts are defined as all grid points with positive and negative $\mathbf{u} \cdot \nabla\theta$ at the lowest model level. Panels have different scales on the y axes.

roughness length. Therefore, in OCEANFRIC, the surface cold front attains a temperature gradient more than double that of the surface warm front (Fig. 5a), which is not the case in NOFRIC (Fig. 5b).

As in the simulations of Hines and Mechoso (1993), Figs. 6a,c,e show how the cyclone structure changes from a Shapiro–Keyser-type cyclone (Shapiro and Keyser 1990), characterized by a bent-back warm front and warm seclusion, in NOFRIC to a Norwegian-type cyclone (Bjerknes 1919; Bjerknes and Solberg 1922), characterized by a thermal ridge and dominant cold front, in LANDFRIC. This contrast in frontal structure between simulations reflects how warm advection dominates without surface friction, so that the warm air moves a long way poleward and wraps around the low center. By contrast, when friction is included, the warm front is broader and weaker, so that the cold front becomes strong relative to the warm front and lies behind a very narrow warm sector.

b. Sensitivity of precipitation bands to roughness length

The consequences of the above differences in cyclone structure on the precipitation bands are as follows. In all simulations, the wide warm-frontal band forms with the synoptic-scale warm advection and extends equatorward as the cyclone begins to occlude (Figs. 6a,c,e). Because in NOFRIC the narrow vertical-velocity maximum, w2 (as shown in OCEANFRIC in Figs. 3 and 4), is along the bent-back warm front (Figs. 6a,b) and therefore close to the wide warm-frontal precipitation band, it does not form a separate precipitation band (Fig. 6a). By contrast, in simulations with friction, w2 develops equatorward along the surface cold front and forms the narrow precipitation band (Figs. 6c,e). However, at 20-km grid spacing, the narrow band is poorly resolved.

Simulations at 20-km grid spacing are shown here because this paper is concerned with bands spaced a few hundreds of kilometers apart. Therefore, additional features that higher-resolution simulations may resolve are generally not of interest. However, in this instance, 20-km grid spacing is limited in producing a band of interest.[2] Therefore, to resolve the narrow band, nests of 4-km grid spacing were inserted in each simulation at the locations indicated by the boxes in Figs. 6a,c,e. In NOFRIC, the precipitation maximum at the triple point remains within the wide warm-frontal band (Fig. 7a). In OCEANFRIC, the narrow band does separate and achieves a much greater precipitation rate than the wide band (Fig. 7b). In LANDFRIC, the two bands are farther apart and the narrow band is more intense (Fig. 7c) than in OCEANFRIC.

Although this greater horizontal distance between the two bands as roughness length increases between simulations is poorly demonstrated in the 20-km simulations (Figs. 6a,c,e), the 20-km simulations demonstrate that w1 and w2 are increasingly separated between simulations (Figs. 6b,d,f). In LANDFRIC, there is a large distance between w1 and w2 and there is a larger separation between their respective humidity maxima than in the other simulations.

The 20-km simulations are also sufficient to demonstrate that the intensification of the narrow band with increasing roughness length between simulations (Fig. 7) is due to the corresponding intensification of w2 between simulations (Figs. 6b,d,f). In LANDFRIC, w2 has intensified to the extent that a prominent gravity wave has been generated above and behind the surface cold front. However, the gravity wave's vertical-velocity anomalies are in the dry air above the cloud head

[2] All other bands documented in this study are qualitatively similar in nests of 4-km grid spacing, inserted at the relevant times and in the relevant locations (not shown).

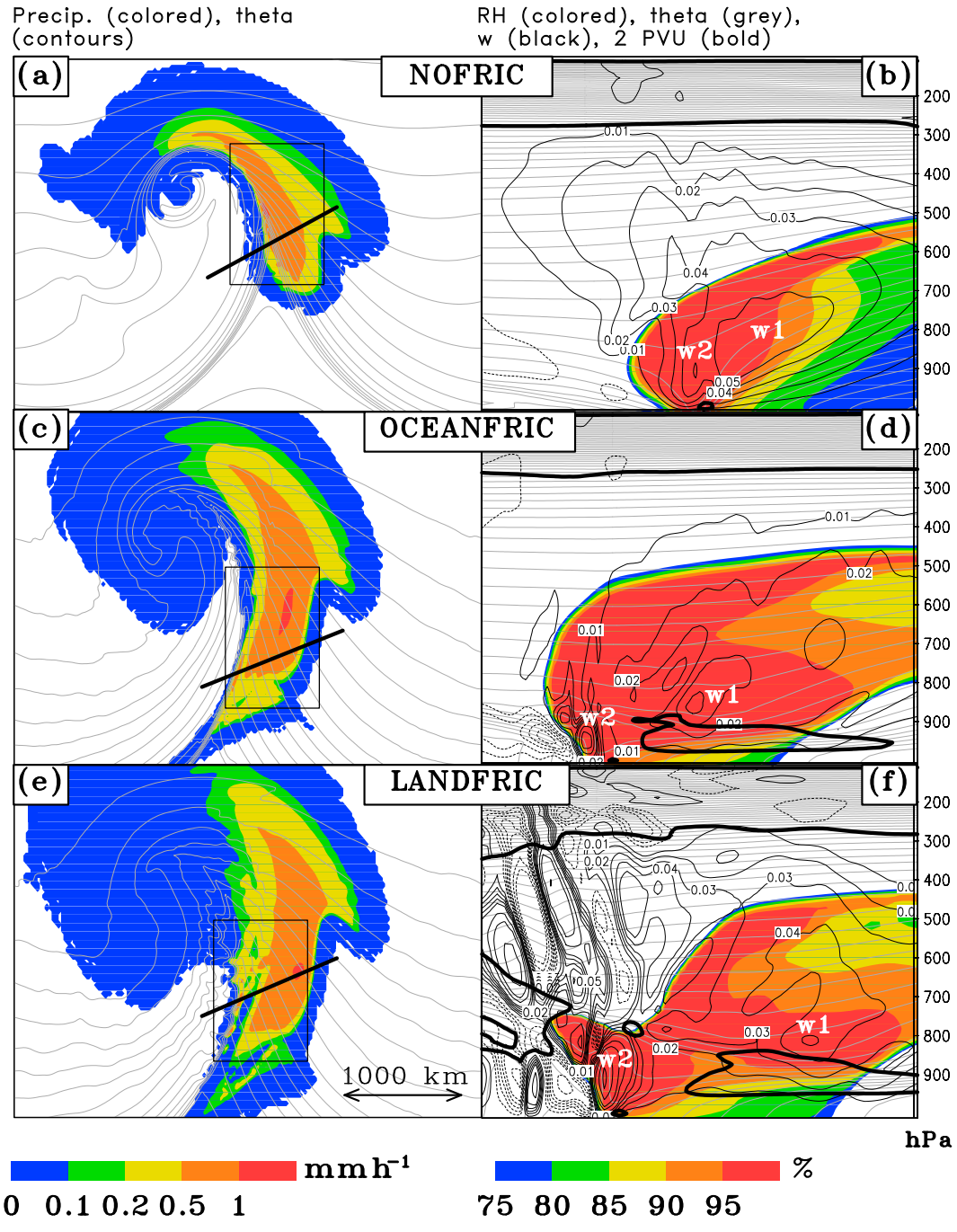

FIG. 6. Comparison between NOFRIC (at 114 h), OCEANFRIC (at 144 h), and LANDFRIC (at 162 h), when a narrow rainband is at its best defined (if it forms at all). Simulations are presented at different times to one another to allow for slower evolution of bands with increasing roughness length. (a),(c),(e) As in Fig. 3, but without wind vectors, for clarity of precipitation features. (b),(d),(f) As in Fig. 3, but with additional w contours of 0.15, 0.2, 0.25, and 0.3 m s^{-1} to emphasize stronger ascent at the surface with increasing roughness length. Boxes drawn in left-hand panels show the locations of the plots at 4-km grid spacing in Fig. 7.

and so do not lead to condensation or precipitation [Plougonven and Snyder (2007) discuss the sensitivity of inertia–gravity waves in WRF idealized baroclinic-wave simulations].

Thus, although w2 initially forms in all simulations in the same manner to that shown for OCEANFRIC in Fig. 4 (not shown for NOFRIC or LANDFRIC), the subsequent intensity and location of its associated precipitation

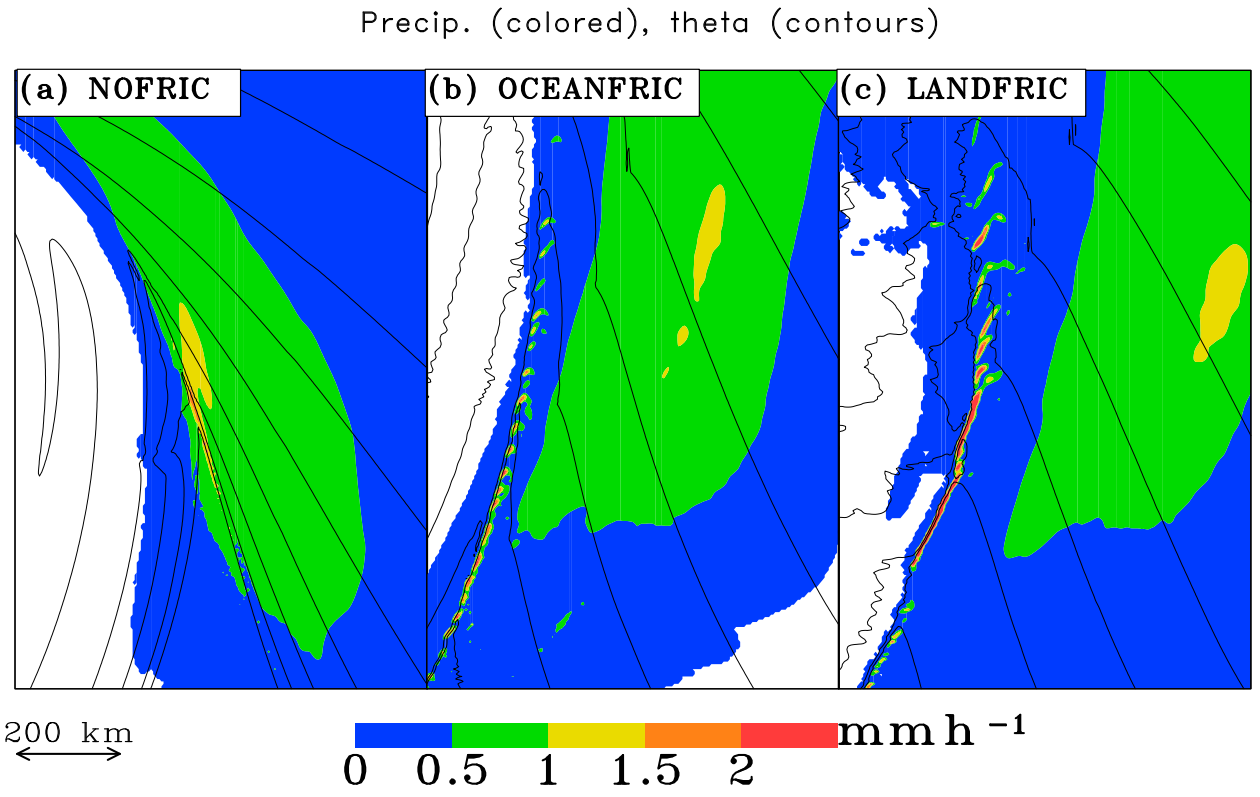

FIG. 7. Comparison of nested domains in (a) NORFRIC, (b) OCEANFRIC, and (c) LANDFRIC at 4-km grid spacing, at times and locations indicated by boxes in Fig. 6. Panels show colored surface precipitation rate (mm h^{-1}, note different scale to previous figures) and black contours of surface θ, with contour interval increased from previous figures to 5 K, so as not to mask the narrow band. Nested domains extend well beyond the area shown, have exactly the same physics as their parent domains, and are all initialized 6 h prior to time shown.

maximum relative to the wide warm-frontal band depends on the roughness length. In these simulations, surface friction enhances multiple banding and, although not quite resolving the narrow band, the 20-km simulations capture the mechanisms by which this multiple banding is enhanced.

These effects of surface friction are consistent with the previous literature. First, the narrow band is of greater magnitude with increasing roughness length between simulations, despite a weaker surface cold front, because the introduction of surface friction and a boundary layer induces frictional convergence at the surface cold front (e.g., Bond and Fleagle 1985; Knight and Hobbs 1988; Bénard et al. 1992a), which is enhanced when the lower boundary is rougher. Second, surface friction retards the eastward motion of the surface cold front (e.g., Braun et al. 1997, 1999; Doyle 1997). The narrow band's eastward motion is also retarded, while bands driven by winds farther aloft are less affected. Thus, there is a greater horizontal distance between bands forced at the surface and those forced at midlevels.

5. Enhancement of warm-sector bands by latent heating

We now focus on the period of OCEANFRIC beyond that shown in Fig. 3, after the low has fully deepened (the time subsequent to that marked by the crisscrosses in Fig. 2), and compare it to LATENT (in which latent heating and cooling, hereafter, just "latent heat," is switched on). Section 5a documents the formation of multiple bands along the warm conveyor belt in both simulations, and section 5b documents the dissipation of those bands.

a. *Formation of multiple bands*

After 162 h in OCEANFRIC, w2 is no longer saturated (Fig. 8b, cf. to the earlier time in Fig. 6d, where w2 is within the moist region). The precipitation is falling ahead of the surface cold front, as in the idealized baroclinic wave of Boutle et al. (2010), and is broadly speaking in the form of a single wide band along the warm conveyor belt (Fig. 8a). This band has evolved from the wide warm-frontal band exhibited in Fig. 3, but is hereafter termed a warm-sector band because there is no distinctive warm

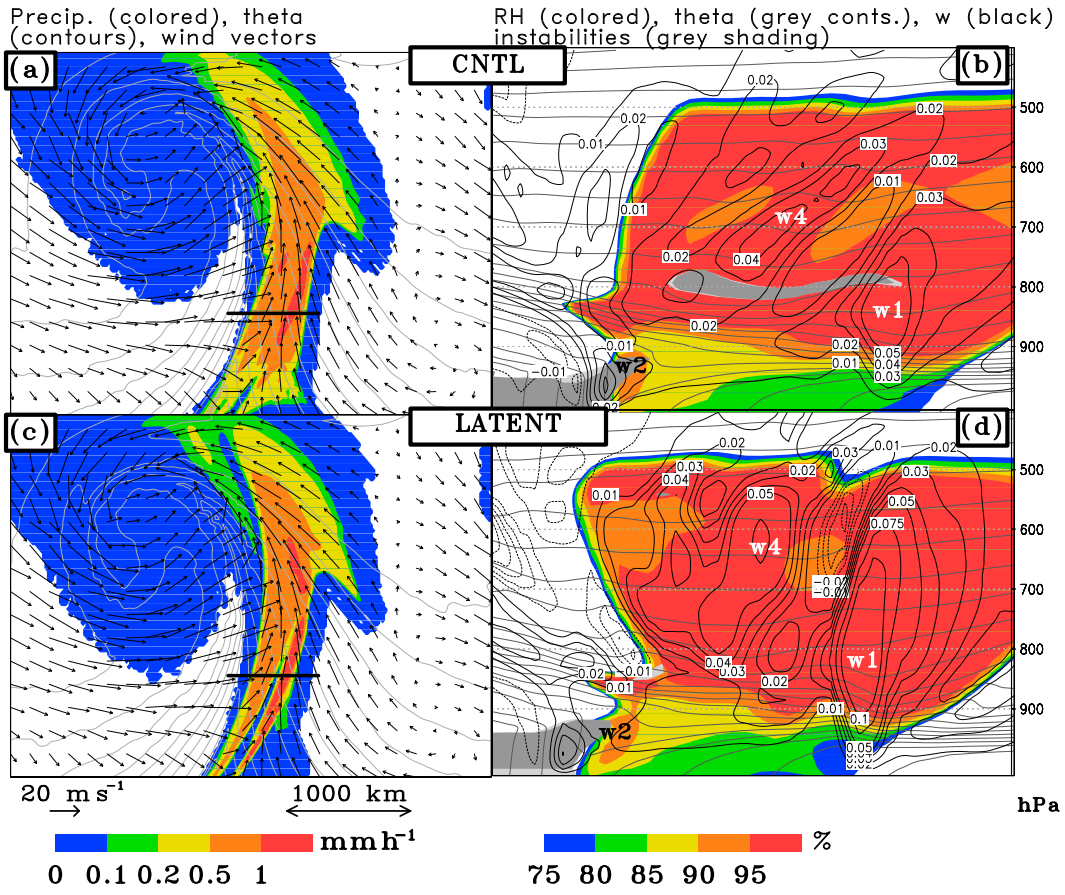

FIG. 8. Comparison between (a),(b) OCEANFRIC and (c),(d) LATENT at mature stage (162 h into simulations). Left-hand panels are as in Fig. 3. Right-hand panels are as in Fig. 3, but no PV is drawn and cross section only goes up to 400 hPa in order to emphasize midtropospheric ascent. Also plotted in right-hand panels are negative moist PV $[(1/\rho)\boldsymbol{\zeta} \cdot \nabla\theta_{es}$, light gray shading, where ρ is density, $\boldsymbol{\zeta}$ is the 3D absolute-vorticity vector, and θ_{es} is equivalent saturated potential temperature]; and negative $\partial\theta_{es}/\partial z$ (indicating conditional instability, dark gray shading).

front at this stage of the simulation. This warm-sector band has developed equatorward, as shown in Fig. 3, and, as in the simulations of Bénard et al. (1992a), persisted beyond the dissipation of the narrow band (in what they term the ''no upright convection stage''). Thus, the cold front has become of the katafront variety (e.g., Bergeron 1937; Sansom 1951; Browning and Monk 1982).

A precipitation maximum is on the east side of the wide warm-sector band (Fig. 8a). A cross section across the warm conveyor belt (Fig. 8b) reveals that w1 (the original wide warm-frontal vertical-velocity maximum) has evolved into a double maximum aloft, w1 and w4. A vertical-velocity and humidity minimum lies between them, and another maximum is beginning to form behind w4.

These two vertical-velocity maxima, w1 and w4, correspond to the poorly defined double-precipitation band in Fig. 8a. By contrast, in LATENT, there is a clear separation between two warm-sector precipitation bands (Fig. 8c). The eastern band is where the release of latent heat has made w1 narrower, more upright, and of greater magnitude (cf. Figs. 8b and 8d). The western band corresponds to the vertical-velocity and humidity maximum, w4. In contrast to OCEANFRIC, the vertical-velocity and humidity minimum between w1 and w4 is a maximum of descent, rather than a minimum of ascent (cf. Figs. 8b and 8d).

The enhancement of these positive and negative vertical-velocity anomalies in LATENT is illustrated by a strip of conditional instability in OCEANFRIC at about 800 hPa (Fig. 8b) that does not appear in LATENT (Fig. 8d) because the instability has been released. All negative moist PV within this midlevel ascent in OCEANFRIC is associated with conditional instability. Therefore, the release of CSI does not appear to have been relevant in forming these multiple bands, nor is there such evidence for any other bands simulated in this study being associated with the release of CSI.

The enhancement of vertical-velocity maxima and reduction of their horizontal scale by latent-heat release was described by Thorpe and Emanuel (1985). In LATENT, these effects have enhanced a wavelike perturbation in vertical velocity across the warm conveyor belt, producing multiple precipitation bands. This perturbation is consistent with the warm-sector band of vertical velocity of Lafore et al. (1994), and that of Zhang and Cho (1995), both of which also exhibited a double maximum at a similar stage of the cyclone life cycle.

Xu (1992) also found that latent-heat release can enhance multiple bands when large-scale moist ascent evolves into substructures. Although these substructures form in OCEANFRIC (i.e., in the absence of latent heat), the substructures are magnified and increasingly separated horizontally when latent-heat release is included. Therefore, these simulations show that there is a tendency for the warm conveyor belt to develop multiple precipitation bands, which is enhanced by latent-heat release, and hence the release of conditional instability, in the mature stage of the cyclone.

In NOFRIC, by this stage of the simulation, the bent-back warm front has intensified and reduced to a scale that does not permit multiple banding on the scale of hundreds of kilometers (not shown). Therefore, friction is required for the warm front to remain at sufficiently large a horizontal scale for these multiple bands to evolve.

b. *Dissipation of multiple bands*

In OCEANFRIC, 30 h later at 192 h, the cyclone (Fig. 2a) and fronts (Fig. 2b) have weakened. The multiple warm-sector bands have evolved into a single band (Fig. 9a). The cross section reveals that the previously discussed wavelike perturbation has decayed so that the vertical velocity within the saturated region has returned to a single maximum, the original w1 (Fig. 9b; the remnant of w4 is marked to illustrate its dissipation).

The addition of latent heat delays the return to a single band, although there is little difference in the magnitude of the low center or fronts at this time (not shown). The double vertical-velocity and humidity maxima are still well defined in LATENT (Fig. 9d) and, thus, there is still a remnant of the double precipitation band (Fig. 9c). As in Fig. 8, the presence of conditional instability collocated with the midlevel ascent in OCEANFRIC (Fig. 9b), but not in LATENT (Fig. 9d), indicates that conditional instability is still being released in LATENT. Thus, latent-heat release continues to enhance the vertical-velocity maxima. Therefore, in these simulations, latent-heat release enhances multiple bands in the warm sector and increases their longevity.

6. Enhancement of anafront by surface fluxes

This section looks at the effects of adding surface heat and moisture fluxes to LATENT. We focus on the same period of the simulations as that in section 5. Section 6a looks at FLUX, in which a SST distribution is prescribed to be equal to the initial temperature of the lowest model level, and compares it to LATENT. Section 6b looks at the effect of varying the SST.

a. *Addition of surface fluxes*

In FLUX, because a meridionally varying SST distribution is prescribed, increasing baroclinicity leads to increasing heat flux into the atmosphere behind the cold front and increasing heat flux into the ocean in the warm sector (as in, e.g., Sinclair et al. 2010). As long as the low remains deep, this postfrontal warm flux remains large (Fig. 10, FLUX curves). After 162 h, w2 is still intense (Fig. 11f) at a time at which it has considerably weakened in LATENT (Fig. 11b). Thus, unlike LATENT, the warm-sector precipitation is still tied to the surface cold front and is intense there (cf. Figs. 11a and 11e), more closely resembling the classic ana-cold-front model (Sansom 1951).

As further illustration of the ana–kata distinction, in LATENT, the dry intrusion is readily evident in the precipitation field (Fig. 11a), resembling the postocclusion conceptual model of Schultz and Vaughan (2011a,b, their Fig. 14b). The cross section passes through the dry intrusion, showing that the dry stable air associated with the tropopause fold overlies the considerably weakened w2 (Fig. 11b). By contrast, in FLUX, the dry slot is less distinctive (Fig. 11e) and the postfrontal boundary layer is much deeper (Fig. 11f) due to the postfrontal heat flux from the ocean into the atmosphere. Therefore, the tropopause fold does not protrude as low and is well behind w2.

The effect of the ana–kata distinction on the precipitation bands is that w1 and w2 have come much closer together with the surface fluxes (cf. Figs. 11b and 11f). Therefore, although the double vertical-velocity maxima aloft (w1 and w4) do form, as in LATENT, they are underlain by the intense w2. Thus, instead of the double precipitation band that forms in LATENT, there is just a single wide band of intense precipitation along and ahead of the surface cold front (Fig. 11e). In this way, the effect of latent heat producing two separate warm-sector bands (Fig. 8) is reversed by surface fluxes.

b. *Sensitivity to sea surface temperature*

To test the sensitivity of the bands to SST, a further simulation, FLUX–10, was performed. FLUX–10 is equivalent to FLUX, but with SST everywhere and uniformly 10 K lower. There is very little difference between FLUX

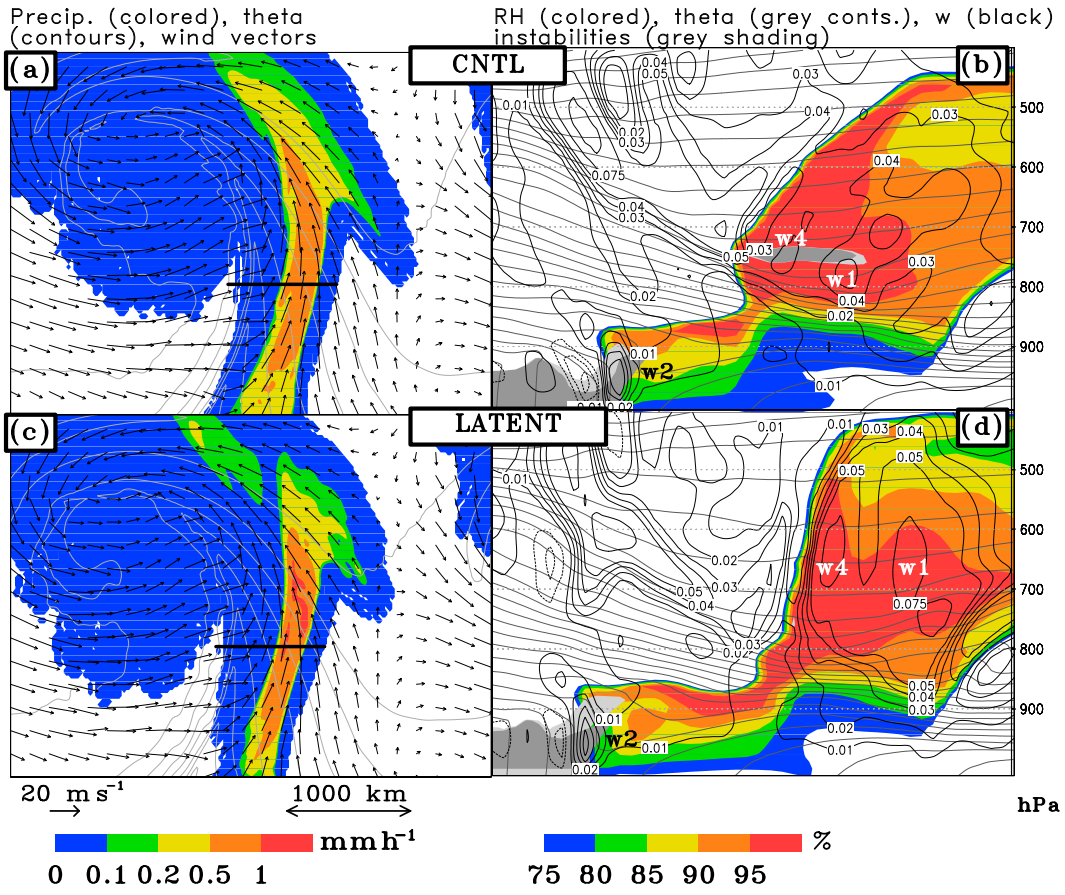

FIG. 9. As in Fig. 8, but after 192 h (30 h later).

and FLUX–10 in the deepening rate of the cyclone, but, in FLUX–10, the maximum surface sensible-heat flux is 30% less than in FLUX (Fig. 10). This contrast is a result of the same air encountering a cooler sea surface at a given grid point in FLUX–10 than in FLUX. Therefore, FLUX–10 can be considered an intermediary between LATENT and FLUX.

FLUX–10 is shown at the same time as LATENT and FLUX in Figs. 11c,d. FLUX–10 bears qualities of each of the other two. The w2 maximum is intense and saturated, as in FLUX, but farther behind the warm-conveyor-belt ascent than in FLUX (cf. Figs. 11d and 11f), allowing more space between w1 and w4. Thus, the double precipitation band has formed (Fig. 11c), albeit less markedly than in LATENT (Fig. 11a).

Prescribing higher SSTs does not completely remove multiple banding, however. In FLUX, 42 h later at 204 h, unlike the other simulations, the precipitation behind the surface cold front has become organized into a number of bands (cf. Figs. 12a, 12c, and 12e) of postfrontal boundary layer convection (e.g., Kuettner 1959; Miura 1986; Atkinson and Zhang 1996) due to enhancement of the postfrontal vertical-velocity and humidity anomalies (cf. Figs. 12b, 12d, and 12f). Therefore, although greater SST inhibits multiple warm-sector bands, it enhances multiple postfrontal bands. This later time of the simulations further illustrates the change from kata-type to ana-type cold front as surface fluxes increase between simulations, with the warm-sector precipitation a long way ahead of the surface cold front in LATENT (Fig. 12a), but still tied to the surface cold front in FLUX (Fig. 12e).

For simplicity, we have used varying SSTs in this work as a proxy for varying surface fluxes. Nonlinearities between the surface layer and lower troposphere mean that real surface fluxes are a complex function of many variables, so our FLUX and FLUX–10 simulations should be taken as a sensitivity test of the model rather than a representation of reality. We include FLUX–10 to illustrate that multiple banding is not precluded by the inclusion of surface fluxes, and that postfrontal bands may not always be present in such simulations.

7. Comparison of simulated bands to observations

The similarity of the bands simulated in this study to other idealized-modeling studies has been noted

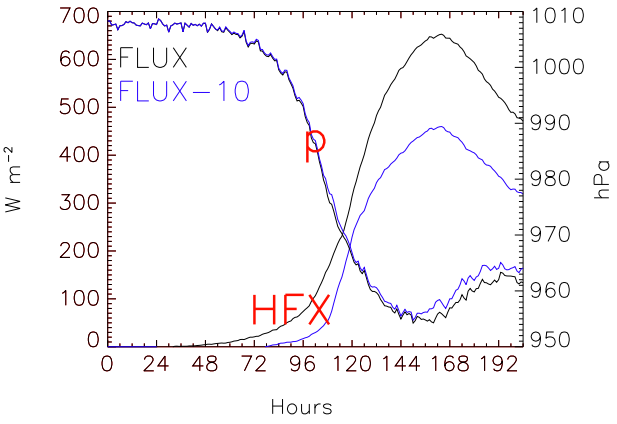

FIG. 10. Time series of domain-maximum surface sensible heat flux (HFX, W m^{-2}) and central surface pressure (p, hPa) in FLUX and FLUX–10. The given heat-flux maximum at all times is in the postfrontal air mass, qualitatively similar to Fig. 1 in Sinclair et al. (2010).

throughout the text. We now discuss how closely these bands resemble those documented in observational studies.

The wide warm-frontal band, the first band to form in all simulations, is a well-documented aspect of extratropical cyclones. As noted by Houze and Hobbs (1982, p. 234), this band forms from "stratiform precipitation produced by widespread lifting associated with warm advection in the leading portion of the cyclone system," which is exactly how it formed in these simulations.

The narrow band, documented in OCEANFRIC and LANDFRIC, results from boundary layer convergence and low static stability above the surface cold front, when the cold front is of an ana type (e.g., Browning and Pardoe 1973; Houze et al. 1976; Hobbs and Biswas 1979; James and Browning 1979; Browning 1986), which is the manner in which the band formed in the simulations with surface friction. Accordingly, the band dissipated in the mature stage of these simulations when the tropopause fold came around the cyclone and overran the band (i.e., when the front changed to kata type).

In the mature stage of the cyclone's evolution, the wide warm-frontal band evolved into multiple warm-sector bands (when latent heat was included). They are termed as such in this paper because there was no distinctive warm front at this stage of the simulations. Such bands have been reported in previous studies. For example, Browning and Harrold (1969, p. 298) observed, from rain gauges, "bands consisting of small rain areas aligned parallel to the warm sector winds" (illustrated in their Fig. 5d). Browning (1986, p. 31) then observed on radar, "organized bands of moderate to heavy rain several tens of kilometers wide. . .associated with mesoscale circulations within the warm conveyor belt about an axis parallel to the relative mean flow" (illustrated in his Fig. 7a). The warm-sector bands in these studies were associated with mature cyclones, as in this paper. The two parallel bands in Fig. 1b are also qualitatively similar to our warm sector bands, lying between the analyzed cold and warm fronts.

The postfrontal bands simulated when surface fluxes were included are also easy to relate to observations. Over open ocean, cold air flowing over warm water generates shallow convection, which is organized into bands, parallel to the vertical shear of the horizontal wind, when that shear is sufficient (e.g., Miura 1986). These postfrontal bands are also exhibited in Fig. 1a, in which the spacing and orientation of the postfrontal bands relative to the principal cold-frontal band closely resemble those in Fig. 12e.

Although all the bands simulated in these experiments are related to similar ones described in the literature, wide cold-frontal bands and wavelike bands (Houze et al. 1976) and prefrontal cold-surge bands (Hobbs 1978) were not simulated, neither were the northwest bands in Novak et al. (2004). We suggest that the explanation may be a result of excluding large-scale deformation in the background flow (e.g., Schultz et al. 1998; Schultz and Zhang 2007) and nonuniform lower-boundary conditions (e.g., Physick 1988; Doyle 1997; Muir and Reeder 2010). Addressing these hypotheses would require further experiments, which are outside the scope of this study.

8. Summary

Moist idealized baroclinic waves were simulated at 20-km grid spacing and the evolution of the associated precipitation bands documented. This study follows up studies of multiple vertical-velocity banding in two-dimensional (e.g., Knight and Hobbs 1988; Bénard et al. 1992a,b; Xu 1992; Lafore et al. 1994; Pizzamei et al. 2005) and three-dimensional (e.g., Zhang and Cho 1995; Gray and Dacre 2008) idealized models. The new elements are the focus on the formation and structure of precipitation bands in a three-dimensional model, and the investigation of sensitivity to a greater variety of physical processes (surface friction, latent-heat release, and surface heat and moisture fluxes).

In all simulations, initially, the vertical-velocity and hence precipitation distribution was driven by synoptic-scale warm advection, leading to a single wide warm-frontal precipitation band (Fig. 3a). As the surface fronts began to develop, a lower-tropospheric lapse-rate maximum developed near the triple point, producing a narrow maximum of vertical velocity within the synoptic-scale ascent.

When the lower boundary was frictionless, the low pressure center deepened and warm advection intensified more than for a rough lower boundary. A Shapiro–Keyser-type cyclone was produced with an intense

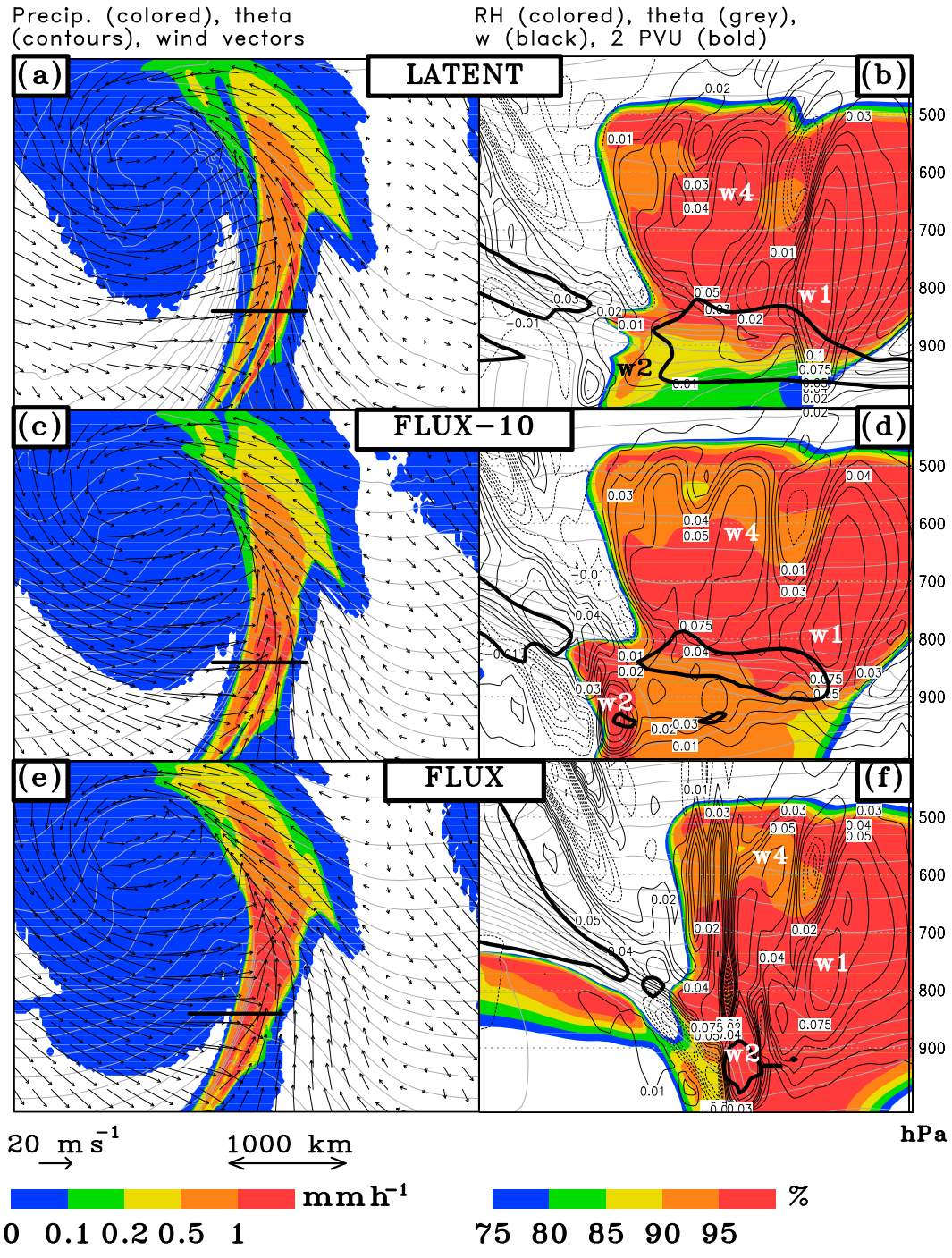

FIG. 11. Comparison at mature stage (162 h into simulations, same time as in Fig. 8) between (a),(b) LATENT, (c),(d) FLUX–10, and (e),(f) FLUX. Left-hand panels are as in Fig. 8. Right-hand panels are as in Fig. 8, but without shaded instabilities and with the dry-PV 2-PVU contour in boldface to emphasize increasing distance between the tropopause fold and w2 with increasing surface fluxes.

bent-back warm front. The precipitation thus became concentrated along the bent-back front. Although a narrow precipitation maximum formed along the bent-back front due to the narrow vertical-velocity maximum, the precipitation maximum did not become a separate band, even in a nested domain of 4-km grid spacing (Fig. 7a). Therefore, multiple bands did not form in the frictionless case.

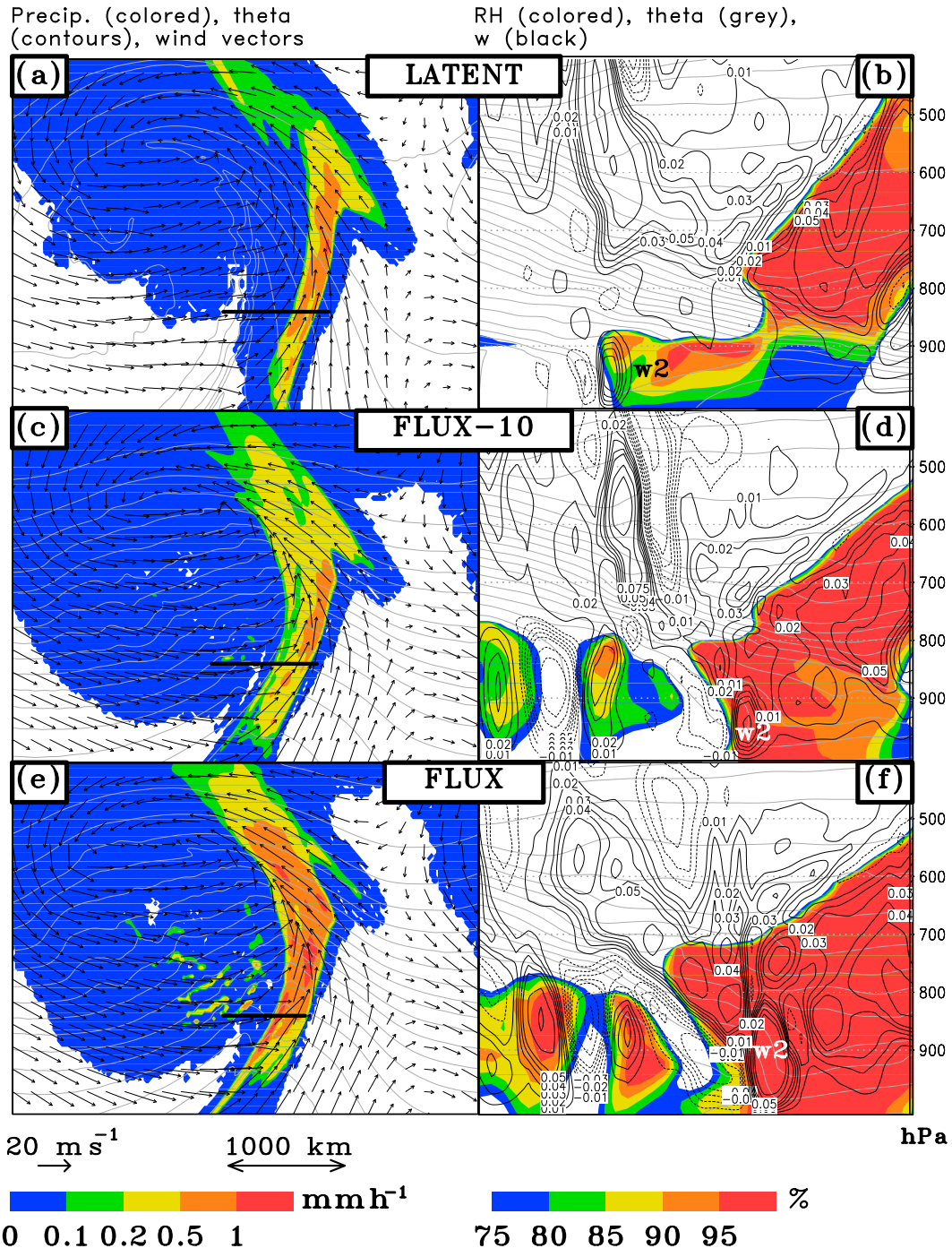

FIG. 12. As in Fig. 11, but after 204 h (42 h later) and the 2-PVU contour is omitted for clarity in the cross sections.

As roughness length was increased to that of an ocean surface in a different simulation, warm advection was reduced and the cold front became stronger relative to the warm front. The narrow vertical-velocity maximum, which in the frictionless case formed along the bent-back front, in this simulation formed along the surface cold front and developed equatorward along the surface cold front. Within the nested domain, this vertical-velocity maximum formed a narrow rainband, separate from the wide warm-frontal band (Fig. 7b).

As roughness length was increased to that of a land surface in a further simulation, a Norwegian-type cyclone

evolved, with the cold front even stronger relative to the warm front. The narrow rainband in the nested domain was more intense due to the greater roughness length, and a greater horizontal distance formed between the narrow band and the wide warm-frontal band (Fig. 7c). Thus, the effect of friction in these simulations was to separate horizontally the two precipitation bands and enhance the narrow band.

In the mature stage of the simulation with roughness length appropriate to the ocean, in the absence of surface fluxes, the surface cold front was overrun by the tropopause fold. The cold front thus became of the katafront variety. The narrow rainband, whose associated ascent was at the surface cold front, thus dissipated and, subsequently, the precipitation distribution became centered on the warm conveyor belt. In the absence of latent-heat release, a wavelike perturbation in vertical velocity and humidity formed across the warm conveyor belt at this stage, but did not produce multiple precipitation bands (Fig. 8a). With the inclusion of latent-heat release, this perturbation became much more pronounced, so that the vertical-velocity maxima were narrower, more upright, and of greater magnitude, and well-defined downdrafts formed between updrafts. Multiple precipitation bands thus developed in the warm sector (Fig. 8c). These bands persisted until the cyclone's low center began to decay, at which point the vertical-velocity and humidity perturbations also decayed and the multiple bands dissipated.

The warm-sector precipitation remained tied to an anatype cold front when surface fluxes were included, with the cold front itself moving at a greater rate eastward than in the simulations without surface fluxes. The postfrontal boundary layer was much deeper, and the tropopause fold did not protrude so low and stayed well behind the surface cold front. Thus, the ascent associated with the narrow rainband remained intense throughout this mature stage of the cyclone. Although multiple vertical-velocity maxima were generated aloft, as in the absence of surface fluxes, they were underlain by the still-intense ascent at the surface cold front. Therefore, a single intense precipitation band lay along and ahead of the surface cold front (Fig. 11e), to which both the surface-based and midtropospheric ascent contributed. However, finer-scale postfrontal bands were generated during this stage of the cyclone's life cycle (Fig. 12e) that did not form in the absence of surface fluxes. When the SST was decreased by 10 K, the simulation more closely resembled the no-surface-fluxes case: multiple warm-sector bands did form and postfrontal bands did not form. Therefore, the inclusion of surface fluxes in baroclinic-wave simulations does not preclude the multiple warm-sector bands, nor does it make the postfrontal bands inevitable.

These simulations show the relative importance of surface friction, latent-heat release, and surface heat and moisture fluxes on the distribution of precipitation within extratropical cyclones. Further idealized-modeling studies with different initial and lower-boundary conditions are needed to show banding tendencies for more specific cyclone types and in specific geographic locations.

Acknowledgments. This work made use of the facilities of HECToR, the United Kingdom's national high-performance computing service (now superceded by ARCHER), which was provided by UoE HPCx Ltd at the University of Edinburgh, Cray Inc, and NAG Ltd., and funded by the Office of Science and Technology through EPSRC's High End Computing Programme. The precipitation-radar data plotted in Fig. 1 were provided by the Met Office through the British Atmospheric Data Centre (BADC). Thanks to Riwal Plougonven, who provided the code to produce the initial jet, and Tim Slater, who altered the code to produce a jet at 20-km grid spacing. We also thank the two anonymous reviewers and Ron McTaggart-Cowan whose comments have improved the manuscript. This work was done while Jesse Norris was a NERC-funded student through the Diabatic Influences on Mesoscale Structures in Extratropical Storms (DIAMET) project, NE/I005234/1.

REFERENCES

Adamson, D. S., S. E. Belcher, B. J. Hoskins, and R. S. Plant, 2006: Boundary-layer friction in midlatitude cyclones. *Quart. J. Roy. Meteor. Soc.,* **132,** 101–124, doi:10.1256/qj.04.145.

Atkinson, B. W., and J. W. Zhang, 1996: Mesoscale shallow convection in the atmosphere. *Rev. Geophys.,* **34,** 403–431, doi:10.1029/96RG02623.

Bénard, P., J. L. Redelsperger, and J. P. Lafore, 1992a: Nonhydrostatic simulation of frontogenesis in a moist atmosphere. Part I: General description and narrow rainbands. *J. Atmos. Sci.,* **49,** 2200–2217, doi:10.1175/1520-0469(1992)049<2200:NSOFIA>2.0.CO;2.

——, J. P. Lafore, and J. L. Redelsperger, 1992b: Nonhydrostatic simulation of frontogenesis in a moist atmosphere. Part II: Moist potential vorticity budget and wide rainbands. *J. Atmos. Sci.,* **49,** 2218–2235, doi:10.1175/1520-0469(1992)049<2218:NSOFIA>2.0.CO;2.

Bennetts, D. A., and B. J. Hoskins, 1979: Conditional symmetric instability—A possible explanation for frontal rainbands. *Quart. J. Roy. Meteor. Soc.,* **105,** 945–962, doi:10.1002/qj.49710544615.

Bergeron, T., 1937: On the physics of fronts. *Bull. Amer. Meteor. Soc.,* **18,** 265–275.

Bjerknes, J., 1919: On the structure of moving cyclones. *Geofys. Publ.,* **1** (2), 1–8.

——, and H. Solberg, 1922: Life cycle of cyclones and the polar front theory of atmospheric circulation. *Geofys. Publ.,* **3** (1), 3–18.

Bond, N. A., and R. G. Fleagle, 1985: Structure of a cold front over the ocean. *Quart. J. Roy. Meteor. Soc.,* **111,** 739–759, doi:10.1002/qj.49711146905.

Boutle, I. A., R. J. Beare, S. E. Belcher, A. R. Brown, and R. S. Plant, 2010: The moist boundary layer under a mid-latitude weather system. *Bound.-Layer Meteor.,* **134,** 367–386, doi:10.1007/s10546-009-9452-9.

Braun, S. A., R. A. Houze Jr., and B. F. Smull, 1997: Airborne dual-Doppler observations of an intense frontal system approaching the Pacific Northwest coast. *Mon. Wea. Rev.,* **125,** 3131–3156, doi:10.1175/1520-0493(1997)125<3131:ADDOOA>2.0.CO;2.

——, R. Rotunno, and J. B. Klemp, 1999: Effects of coastal orography on landfalling cold fronts. Part II: Effects of surface friction. *J. Atmos. Sci.,* **56,** 3366–3384, doi:10.1175/1520-0469(1999)056<3366:EOCOOL>2.0.CO;2.

Browning, K. A., 1986: Conceptual models of precipitation systems. *Wea. Forecasting,* **1,** 23–41, doi:10.1175/1520-0434(1986)001<0023:CMOPS>2.0.CO;2.

——, 1990: Organization of clouds and precipitation in extratropical cyclones. *Extratropical Cyclones: The Erik Palmén Memorial Volume,* C. W. Newton and E. O. Holopainen, Eds., Amer. Meteor. Soc., 129–153.

——, 2005: Observational synthesis of mesoscale structures within an explosively developing cyclone. *Quart. J. Roy. Meteor. Soc.,* **131,** 603–623, doi:10.1256/qj.03.201.

——, and T. W. Harrold, 1969: Air motion and precipitation growth in a wave depression. *Quart. J. Roy. Meteor. Soc.,* **95,** 288–309, doi:10.1002/qj.49709540405.

——, and C. W. Pardoe, 1973: Structure of low-level jet streams ahead of mid-latitude cold fronts. *Quart. J. Roy. Meteor. Soc.,* **99,** 619–638, doi:10.1002/qj.49709942204.

——, and G. A. Monk, 1982: A simple model for the synoptic analysis of cold fronts. *Quart. J. Roy. Meteor. Soc.,* **108,** 435–452, doi:10.1002/qj.49710845609.

——, and N. M. Roberts, 1999: Mesoscale analysis of arc rain bands in a dry slot. *Quart. J. Roy. Meteor. Soc.,* **125,** 3495–3511, doi:10.1002/qj.49712556118.

——, M. E. Hardman, T. W. Harrold, and C. W. Pardoe, 1973: The structure of rainbands within a mid-latitude depression. *Quart. J. Roy. Meteor. Soc.,* **99,** 215–231, doi:10.1002/qj.49709942002.

——, N. M. Roberts, and I. J. Illingworth, 1997: Mesoscale analysis of the activation of a cold front during cyclogenesis. *Quart. J. Roy. Meteor. Soc.,* **123,** 2349–2375, doi:10.1002/qj.49712354410.

Carlson, T. N., 1980: Airflow through midlatitude cyclones and the comma cloud pattern. *Mon. Wea. Rev.,* **108,** 1498–1509, doi:10.1175/1520-0493(1980)108<1498:ATMCAT>2.0.CO;2.

Cooper, I. M., A. J. Thorpe, and C. H. Bishop, 1992: The role of diffusive effects on potential vorticity in fronts. *Quart. J. Roy. Meteor. Soc.,* **118,** 629–647, doi:10.1002/qj.49711850603.

Doyle, J. D., 1997: The influence of mesoscale orography on a coastal jet and rainband. *Mon. Wea. Rev.,* **125,** 1465–1488, doi:10.1175/1520-0493(1997)125<1465:TIOMOO>2.0.CO;2.

Gray, S. L., and H. F. Dacre, 2008: The impact of deformation strain on the formation of banded clouds in idealized modelling experiments. *Quart. J. Roy. Meteor. Soc.,* **134,** 859–874, doi:10.1002/qj.262.

Heymsfield, G. M., 1979: Doppler radar study of a warm frontal region. *J. Atmos. Sci.,* **36,** 2093–2107, doi:10.1175/1520-0469(1979)036<2093:DRSOAW>2.0.CO;2.

Hines, K. M., and C. R. Mechoso, 1993: Influence of surface drag on the evolution of fronts. *Mon. Wea. Rev.,* **121,** 1152–1175, doi:10.1175/1520-0493(1993)121<1152:IOSDOT>2.0.CO;2.

Hobbs, P. V., 1978: Organization and structure of clouds and precipitation on the mesoscale and microscale in cyclonic storms. *Rev. Geophys. Space Phys.,* **16,** 741–755, doi:10.1029/RG016i004p00741.

——, and K. R. Biswas, 1979: The cellular structure of narrow cold-frontal rainbands. *Quart. J. Roy. Meteor. Soc.,* **105,** 723–727, doi:10.1002/qj.49710544516.

Holton, J. R., and G. J. Hakim, 2013: *An Introduction to Dynamic Meteorology.* 5th ed. Academic Press, 532 pp.

Hong, S.-Y., Y. Noh, and J. Dudhia, 2006: A new vertical diffusion package with an explicit treatment of entrainment processes. *Mon. Wea. Rev.,* **134,** 2318–2341, doi:10.1175/MWR3199.1.

Hoskins, B. J., E. Caetano Neto, and H. R. Cho, 1984: The formation of multiple fronts. *Quart. J. Roy. Meteor. Soc.,* **110,** 881–896, doi:10.1002/qj.49711046606.

Houze, R. A., Jr., and P. V. Hobbs, 1982: Organization and structure of precipitating cloud systems. *Advances in Geophysics,* Vol. 24, Academic Press, 225–315, doi:10.1016/S0065-2687(08)60521-X.

——, ——, K. R. Biswas, and W. M. Davis, 1976: Mesoscale rainbands in extratropical cyclones. *Mon. Wea. Rev.,* **104,** 868–878, doi:10.1175/1520-0493(1976)104<0868:MRIEC>2.0.CO;2.

James, P. K., and K. A. Browning, 1979: Mesoscale structure of line convection at surface cold fronts. *Quart. J. Roy. Meteor. Soc.,* **105,** 371–382, doi:10.1002/qj.49710544404.

Kain, J. S., 2004: The Kain–Fritsch convective parameterization: An update. *J. Appl. Meteor.,* **43,** 170–181, doi:10.1175/1520-0450(2004)043<0170:TKCPAU>2.0.CO;2.

Knight, D. J., and P. V. Hobbs, 1988: The mesoscale and microscale structure and organization of clouds and precipitation in midlatitude cyclones. Part XV: A numerical modeling study of frontogenesis and cold-frontal rainbands. *J. Atmos. Sci.,* **45,** 915–930, doi:10.1175/1520-0469(1988)045<0915:TMAMSA>2.0.CO;2.

Kuettner, J., 1959: The band structure of the atmosphere. *Tellus,* **11A,** 267–294, doi:10.1111/j.2153-3490.1959.tb00033.x.

Lafore, J. P., J. L. Redelsperger, C. Cailly, and E. Arbogast, 1994: Nonhydrostatic simulation of frontogenesis in a moist atmosphere. Part III: Thermal wind imbalance and rainbands. *J. Atmos. Sci.,* **51,** 3467–3485, doi:10.1175/1520-0469(1994)051<3467:NSOFIA>2.0.CO;2.

Miura, Y., 1986: Aspect ratios of longitudinal rolls and convection cells observed during cold air outbreaks. *J. Atmos. Sci.,* **43,** 26–39, doi:10.1175/1520-0469(1986)043<0026:AROLRA>2.0.CO;2.

Monin, A. S., and A. M. Obukhov, 1954: Basic laws of turbulent mixing in the surface layer of the atmosphere. *Tr. Geofiz. Inst., Akad. Nauk SSSR,* **24,** 163–187.

Muir, L. C., and M. J. Reeder, 2010: Idealized modelling of landfalling cold fronts. *Quart. J. Roy. Meteor. Soc.,* **136,** 2147–2161, doi:10.1002/qj.692.

Novak, D. R., and B. A. Colle, 2012: Diagnosing snowband predictability using a multimodel ensemble system. *Wea. Forecasting,* **27,** 565–585, doi:10.1175/WAF-D-11-00047.1.

——, L. F. Bosart, D. Keyser, and J. S. Waldstreicher, 2004: An observational study of cold season–banded precipitation in Northeast U.S. cyclones. *Wea. Forecasting,* **19,** 993–1010, doi:10.1175/815.1.

——, B. A. Colle, and A. R. Aiyyer, 2010: Evolution of mesoscale precipitation band environments within the comma head of Northeast U.S. cyclones. *Mon. Wea. Rev.,* **138,** 2354–2374, doi:10.1175/2010MWR3219.1.

Parsons, D. B., and P. V. Hobbs, 1983: The mesoscale and microscale structure and organization of clouds and precipitation in midlatitude cyclones. VII: Formation, development, interaction and dissipation of rainbands. *J. Atmos. Sci.,* **40,** 559–579, doi:10.1175/1520-0469(1983)040<0559:TMAMSA>2.0.CO;2.

Physick, W. L., 1988: Mesoscale modeling of a cold front and its interaction with a diurnally heated land mass. *J. Atmos.*

Sci., **45,** 3169–3187, doi:10.1175/1520-0469(1988)045<3169:MMOACF>2.0.CO;2.

Pizzamei, M., S. L. Gray, and K. A. Browning, 2005: Cloud-resolving model simulations of multiply-banded frontal clouds. *Quart. J. Roy. Meteor. Soc.,* **131,** 2617–2637, doi:10.1256/qj.04.175.

Plougonven, R., and C. Snyder, 2007: Inertia–gravity waves spontaneously generated by jets and fronts. Part I: Different baroclinic life cycles. *J. Atmos. Sci.,* **64,** 2502–2520, doi:10.1175/JAS3953.1.

Rotunno, R., W. C. Skamarock, and C. Snyder, 1994: An analysis of frontogenesis in numerical simulations of baroclinic waves. *J. Atmos. Sci.,* **51,** 3373–3398, doi:10.1175/1520-0469(1994)051<3373:AAOFIN>2.0.CO;2.

——, ——, and ——, 1998: Effects of surface drag on fronts within numerically simulated baroclinic waves. *J. Atmos. Sci.,* **55,** 2119–2129, doi:10.1175/1520-0469(1998)055<2119:EOSDOF>2.0.CO;2.

Sansom, H. W., 1951: A study of cold fronts over the British Isles. *Quart. J. Roy. Meteor. Soc.,* **77,** 96–120, doi:10.1002/qj.49707733111.

Schultz, D. M., and P. N. Schumacher, 1999: The use and misuse of conditional symmetric instability. *Mon. Wea. Rev.,* **127,** 2709–2732; Corrigendum, **128,** 1573.

——, and J. A. Knox, 2007: Banded convection caused by frontogenesis in a conditionally, symmetrically, and inertially unstable environment. *Mon. Wea. Rev.,* **135,** 2095–2110, doi:10.1175/MWR3400.1.

——, and F. Zhang, 2007: Baroclinic development within zonally-varying flows. *Quart. J. Roy. Meteor. Soc.,* **133,** 1101–1112, doi:10.1002/qj.87.

——, and G. Vaughan, 2011a: Occluded fronts and the occlusion process: A fresh look at conventional wisdom. *Bull. Amer. Meteor. Soc.,* **92,** 443–466, doi:10.1175/2010BAMS3057.1.

——, and ——, 2011b: Occluded fronts and the occlusion process: A fresh look at conventional wisdom. *Bull. Amer. Meteor. Soc.,* **92** (Suppl.), doi:10.1175/2010BAMS3057.2.

——, D. Keyser, and L. F. Bosart, 1998: The effect of large-scale flow on low-level frontal structure and evolution in mid-latitude cyclones. *Mon. Wea. Rev.,* **126,** 1767–1791, doi:10.1175/1520-0493(1998)126<1767:TEOLSF>2.0.CO;2.

Schumacher, R. S., D. M. Schultz, and J. A. Knox, 2010: Convective snowbands downstream of the Rocky Mountains in an environment with conditional, dry symmetric, and inertial instabilities. *Mon. Wea. Rev.,* **138,** 4416–4438, doi:10.1175/2010MWR3334.1.

Seltzer, M. A., R. E. Passarelli, and K. A. Emanuel, 1985: The possible role of symmetric instability in the formation of precipitation bands. *J. Atmos. Sci.,* **42,** 2207–2219, doi:10.1175/1520-0469(1985)042<2207:TPROSI>2.0.CO;2.

Shapiro, M. A., and D. Keyser, 1990: Fronts, jet streams and the tropopause. *Extratropical Cyclones: The Erik Palmén Memorial Volume,* C. W. Newton and E. O. Holopainen, Eds., Amer. Meteor. Soc., 167–191.

Sinclair, V. A., S. E. Belcher, and S. L. Gray, 2010: Synoptic controls on boundary-layer characteristics. *Bound.-Layer Meteor.,* **134,** 387–409, doi:10.1007/s10546-009-9455-6.

Skamarock, W. C., and Coauthors, 2008: A description of the Advanced Research WRF version 3. NCAR Tech. Note NCAR/TN–475+STR, 113 pp. [Available online at http://www.mmm.ucar.edu/wrf/users/docs/arw_v3_bw.pdf.]

Thompson, G., P. R. Field, R. M. Rasmussen, and W. D. Hall, 2008: Explicit forecasts of winter precipitation using an improved bulk microphysics scheme. Part II: Implementation of a new snow parameterization. *Mon. Wea. Rev.,* **136,** 5095–5115, doi:10.1175/2008MWR2387.1.

Thorpe, A. J., and K. A. Emanuel, 1985: Frontogenesis in the presence of small stability to slantwise convection. *J. Atmos. Sci.,* **42,** 1809–1824, doi:10.1175/1520-0469(1985)042<1809:FITPOS>2.0.CO;2.

Wolfsberg, D. G., K. A. Emanuel, and R. E. Passarelli, 1986: Band formation in a New England winter storm. *Mon. Wea. Rev.,* **114,** 1552–1569, doi:10.1175/1520-0493(1986)114<1552:BFIANE>2.0.CO;2.

Xu, Q., 1992: Formation and evolution of frontal rainbands and geostrophic potential vorticity anomalies. *J. Atmos. Sci.,* **49,** 629–648, doi:10.1175/1520-0469(1992)049<0629:FAEOFR>2.0.CO;2.

Zhang, D.-L., and H.-R. Cho, 1995: Three-dimensional simulation of frontal rainbands and conditional symmetric instability in the Eady-wave model. *Tellus,* **47A,** 45–61, doi:10.1034/j.1600-0870.1995.00003.x.